

Design Guidelines for Terahertz Mixers and Detectors

Paolo Focardi, William R. McGrath, *Member, IEEE*, and Andrea Neto

Abstract—Twin-slot antennas and coplanar waveguides are a popular choice for coupling signals to state-of-the-art mixers and detectors at terahertz frequencies. Although these sensors show promising performance in terms of noise temperature, they usually also show a considerable downward shift in the center frequency of their spectral response, especially when compared with calculations obtained with commonly used simplified models. In this paper, we describe an accurate and complete electromagnetic model of these detectors, which represents a significant improvement over other published approaches. We present the procedure used to obtain a very good agreement between measurements and calculations at terahertz frequencies both in terms of center frequency and bandwidth. The wide variety of measured and calculated data presented in this paper also demonstrates the effectiveness and reliability of the electromagnetic model in all the investigated frequency bands.

Index Terms—Coplanar waveguide (CPW) lines, hot electron bolometers (HEBs), lens antennas, slot antennas, terahertz frequencies.

I. INTRODUCTION

TWIN SLOT antennas coupled to coplanar waveguides (CPWs) [1], [2] have been developed for quasi-optical single-pixel detectors employed in atmospheric and astronomical instruments in the sub-millimeter-wave/terahertz-frequency range. Hot electron bolometer (HEB) mixers, for example, are often used at terahertz frequencies in such circuits placed at the second focus of a dielectric lens [3], [4]. HEB receivers are already finding use up to 1 THz on ground-based radio telescopes [5], and similar receivers are being developed for frequencies up to 2 THz for the European Space Agency/National Aeronautics Space Administration (ESA/NASA) Herschel Space Observatory,¹ and up to 2 THz for NASA's SOFIA Aircraft Observatory.²

A 600-GHz design was published in 1993 [2] and since then there have been several attempts to scale the same design to much higher frequencies. However, the main problem that afflicted these scaled designs was that the measured center frequency (i.e., frequency of the peak response of the detector)

was often significantly lower than that calculated with simple models [4], [6], which relied on quasi-static approximations for the equivalent-circuit parameters [7]. As shown in [8], the accurate characterization and modeling of the entire mixer embedding circuit, including the parasitics associated with the geometry of the device, is needed to correctly design the circuit. Even though the geometry of these antennas, CPW lines, and devices is relatively simple, simulating the performance in a terahertz circuit is not a straightforward matter. A brute-force approach based on a method of moments (MoM) analysis of the overall planar structure can be used [9], but since the device dimensions can be of the order of $\lambda/1000$, the numerical effort required for an accurate analysis becomes almost prohibitive, even for a single antenna. Therefore, an improved electromagnetic model and computational tools that are accurate enough to correctly design these detectors at the desired center frequency are needed.

In [8], we tackled this problem and discussed the performance of seven different detectors in the range from 500 GHz to 2.5 THz, fabricated following the guidelines of an earlier design. In particular, the formulation takes into account the effect on the input impedance of the components of the circuit that were previously neglected. First, a specialized formulation for the propagation constant of the CPW lines to include the radiation losses was developed. The effect on the embedding impedance of the CPW-to-bolometer transition was then introduced, which explained part of the observed downward shift in the center frequency. Finally, the effect of the RF choke filter on the embedding impedance was modeled. The good agreement of the calculations with the measured results, as shown in [8], demonstrated the practical application of the improved electromagnetic model.

Based on these initial successful results, the model has now been further improved, and a complete new set of terahertz mixers with center frequencies ranging from 600 GHz to 2.5 THz has been designed, fabricated, and tested. Several features have been updated and modified in the new designs and further improvements have been added to the electromagnetic model. While we have used HEBs as the devices to test our terahertz circuit model, the same electromagnetic model is also directly applicable to detectors based on other devices such as superconductor-insulator-superconductor (SIS) mixers or Schottky mixers. The limit of this model is essentially given by its ability to find an appropriate embedding impedance to optimize the device performance. Any impedance in the range between a few ohms and a few hundred ohms is theoretically achievable by the embedding circuit, making this electromagnetic model suitable not only for HEB mixers, but also for SIS and Schottky mixers, covering, therefore, most of the devices used in this frequency range.

Manuscript received July 26, 2004; revised September 14, 2004. This work was supported by the National Aeronautics and Space Administration under a contract.

P. Focardi and W. R. McGrath are with the Jet Propulsion Laboratory, California Institute of Technology, Pasadena, CA 91109 USA (e-mail: Paolo.Focardi@jpl.nasa.gov; William.R.McGrath@jpl.nasa.gov).

A. Neto is with the Center for Applied scientific Research (TNO), TNO Defence and Security, 2597 AK, Den Haag, The Netherlands (e-mail: andrea.neto@tno.nl).

Digital Object Identifier 10.1109/TMTT.2005.847058

¹For further reference see official web page. [Online]. Available: <http://herchel.jpl.nasa.gov>

²For further reference see official web page. [Online]. Available: <http://www.sofia.usra.edu>

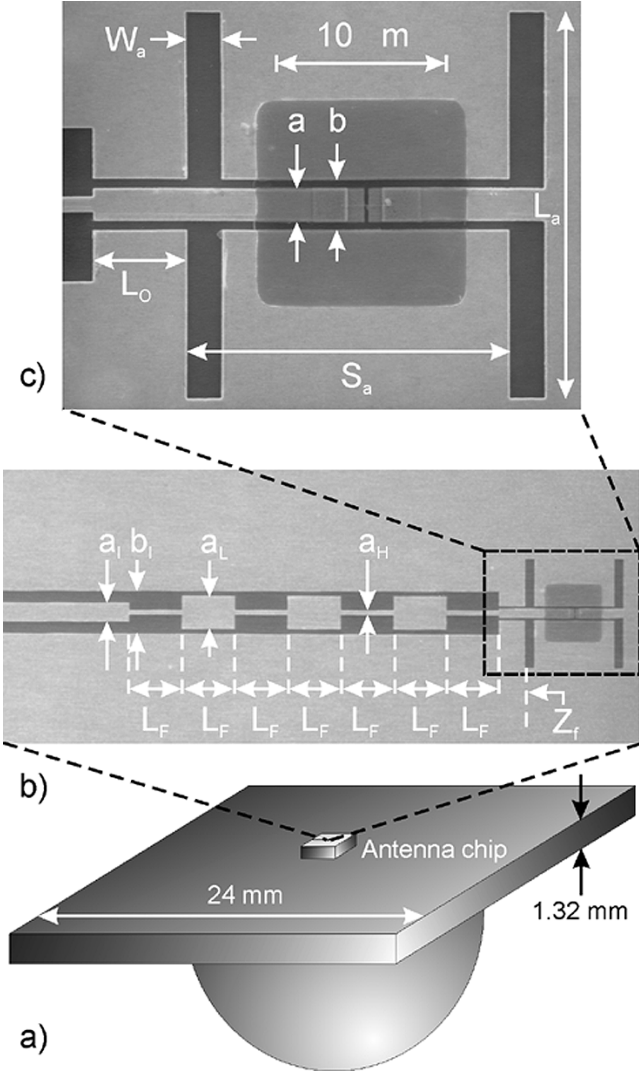


Fig. 1. (a) Three-dimensional (3-D) view of the back of the silicon elliptical lens with its square holding plate and the antenna chip located at the second focus of the lens itself. (b) Overview of the geometry of a 2.5-THz detector embedding circuit. (c) Close-up view of the twin-slot antenna.

In this paper, we demonstrate that the model is now accurate enough not only for the analysis (as shown in [8]), but also for the synthesis of terahertz detectors. In Section II, the geometry of the detector and antenna circuit are briefly described. In Section III, all the features introduced into the electromagnetic model are presented and discussed. In particular, we carefully analyze and model each part of the detector, from the Gaussian beam coupling that occurs outside the silicon lens to the effect of the bolometer transition on the circuit input impedance, in order to calculate the actual power coupling efficiency. In Section IV, the modifications to the new detectors are discussed. The slot-antenna length and, therefore, the resonating frequency, has been changed, a new bolometer-to-CPW transition has been developed, and the length of the sections of the RF choke filter have been tuned to result in the desired center frequency. In Section V, a comparison between predicted and experimental results is presented along with a summary of all measured and calculated data, and finally, in Section VI, we provide some concluding remarks.

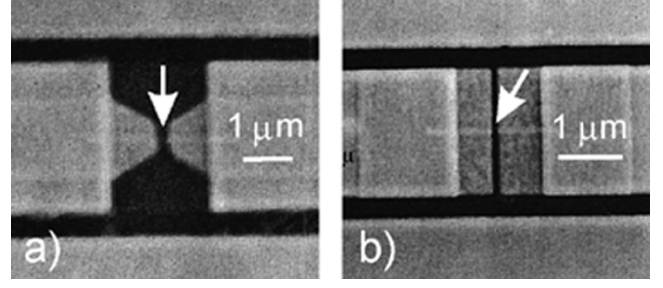


Fig. 2. Scanning electron microscope (SEM) photographs of the two different bolometer-to-CPW transitions adopted for the detectors under investigation. (a) The conventional tapered geometry. (b) The new nontapered design. The arrows indicate the position of the Nb bolometers, which are difficult to see in these photographs.

Freq. [THz]	L_a [μm]	W_a [μm]	S_a [μm]	L_o tapered [μm]	L_o non-tapered [μm]
2.5	23	2	19	7.5	5.5
1.8	32	3	26	10	9
1.6	36	3	29	12	10.5
0.6	96	8	79	27	25

Freq. [THz]	a [μm]	b [μm]	a_H [μm]	a_L [μm]	a_i [μm]	b_i [μm]	L_F [μm]
2.5	2	3	1	7	4	9	11
1.8	3	4	1	7	4	9	13
1.6	3	4	1	7	4	9	14.5
0.6	8	11	2	14	8	18	40

Fig. 3. Summary of geometrical dimensions used in the design of the new detectors. Refer to Fig. 1 for the meaning of the different parameters.

II. DETECTOR GEOMETRY

The detectors under investigation consist of a twin-slot antenna located at the second focus of a silicon elliptical lens. With reference to Fig. 1(a), the lens, whose major semi axis is 6.308 mm, is a half-ellipse plus an extension length of 0.142 mm. This latter is then connected to a square 24-mm 1.32-mm-thick silicon plate used to hold the lens in position in the mixer block. At the center of the square plate is located the 0.381-mm-thick device/embedding-circuit chip, whose lateral dimensions are 1.2×2.4 mm for all the frequency bands, except for the lowest (600 GHz), which uses a square 2.4-mm chip. The detector embedding circuit [see Fig. 1(b)] is etched in a 0.3-μm-thick gold film, which has a measured dc resistivity of $0.55 \mu\Omega \cdot \text{cm}$ at 4.2 K. In Fig. 1(b), from the left-to right-hand side, there is the 50-Ω CPW line that connects the embedding circuit to the rest of the electronics, the RF choke filter with seven high- and low-impedance sections and the twin-slot antenna. A close-up view of the antenna is shown in Fig. 1(c). In this example, the device is a $0.1 \times 0.1 \mu\text{m}$ Nb bolometer with a nontapered transition to the CPW line. The square darker area around the bolometer is a thin layer of SiO_2 used to protect the superconducting Nb bolometer. The details of the two different bolometer-to-CPW transitions used in the new designs are shown in Fig. 2. The shape of the transition has been modified from tapered to nontapered based on the formulation presented in [8]. Both geometries have been fabricated and measured, obtaining, in both cases, good results due to the slightly different designs used to compensate for the transition embedding impedance. In Fig. 3, a summary of the geometrical

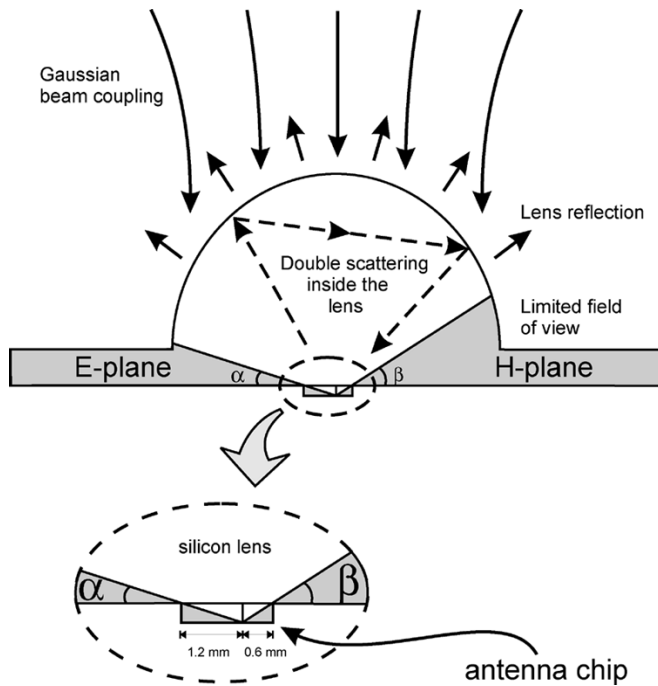


Fig. 4. Sketch of the lens geometry with the different features of the model indicated.

dimensions used in the design of the new detectors is shown. For the different frequency bands (2.5, 1.8, and 1.6 THz and 600 GHz), all the parameter are listed. Note the adjustments made to the values of L_O depending on the transition type. Moreover, two different bolometer lengths have been used, i.e., 0.1 and 0.2 μm (each is 0.1- μm wide), resulting in a complete set of 16 different detectors.

III. MODEL DESCRIPTION

Here, all the different parts of the model are discussed and accurately described. Fig. 4 shows a sketch of the different contributions included in this model. Starting from outside the silicon lens, we describe all the losses an electromagnetic wave sustains along its path until it gets to the bolometer: these include the Gaussian beam coupling between source and silicon lens, the reflection at the lens interface, the double scattering inside the lens (which modifies the slot impedance), and the limited field of view of the antenna due to the dimensions of the antenna chip. Fig. 5 shows the equivalent RF embedding circuit used in the simulations. It resembles the shape of its real counterpart of Fig. 1(c) and shows all the components modeled and described here, i.e., the slot input impedances Z_s and pertinent equivalent generators V_s , the filter impedance Z_f , the impedance of the bolometer transition Z_t , the bolometer resistance R_b , and the characteristic parameters of the CPW line k_0 and Z_0 .

The first effect we model is the coupling efficiency of the detector to a fundamental Gaussian mode that occurs outside the silicon lens. In our measurement setup, we have a Fourier transform spectrometer (FTS) that provides power to our detectors through a multimode optical beam. However, the detector couples only to a single Gaussian mode of the FTS. In calculating the mutual coupling efficiency, between the detector and the FTS, we consider two different beam waists, i.e., 6.25 mm

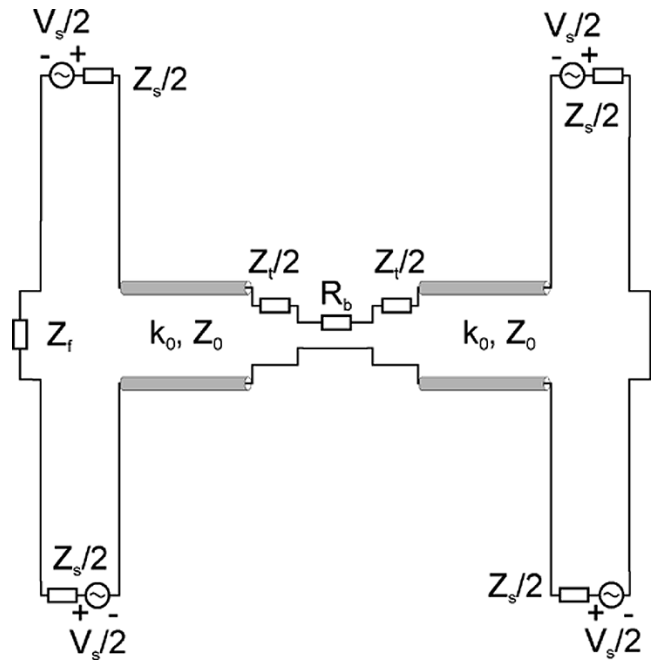


Fig. 5. Equivalent RF circuit used in the simulations.

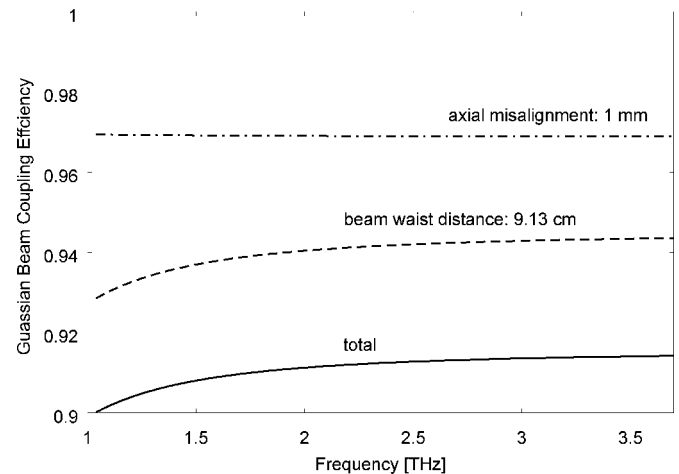


Fig. 6. Power coupling efficiency of the Gaussian beam coupling that occurs outside the silicon lens. The effect of the axial misalignment and of the beam waist distance are plotted separately from the total.

for the FTS and 4.92 mm for the silicon lens. We then introduce the effect of the distance between the beam waists, which, for our measurement setup is 9.13 cm, and also an axial misalignment between the two beams due to a small error in positioning our Dewar on the aperture of the FTS. The simple formulation to account for these parameters can be found in [10]. In Fig. 6, the effect of the Gaussian beam coupling on the power coupling efficiency is shown. In this example, an axial misalignment of 1 mm has been considered along with the proper beam waist distance. Moreover, the two effects are plotted separately from the total contribution. As a result, roughly 9% of the total power in our setup is lost before reaching the silicon lens.

Next, the dielectric interface between free space and the silicon lens surface is considered, and the amount of power that penetrates the lens is calculated with a simple transmission-line model. Due to the fact that our lenses have no antireflection

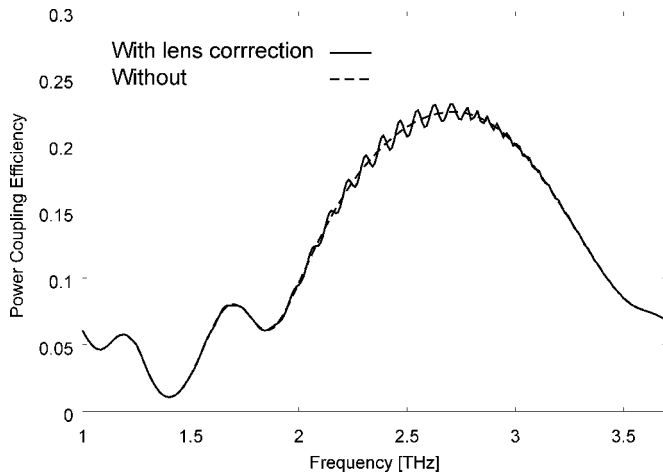


Fig. 7. Effect of the silicon lens on the overall efficiency of the detector. The ripples produced by the lens are often visible in the measurements.

coating, a total of 30% of the power is reflected away across the whole bandwidth of interest. Therefore, in our case, by the time an electromagnetic wave arrives inside the silicon lens, roughly 40% of the total power is already lost.

The application of the MoM in order to obtain the bare input impedance of the twin slots alone is the next step. The MoM code has been first developed in [9] and considers the slots placed at the interface between two semi-infinite dielectrics, silicon, and free space. Once the self and mutual admittances of the twin-slot antenna are known, the effect of every other part of the circuit on the input impedance is then introduced separately.

Once inside the lens, we consider the slot input impedance variation due to the presence of the elliptical silicon lens rather than a semi-infinite medium in front of the twin-slot antenna. Fig. 7 shows this effect, calculated following the same procedure presented in [11] and [12]. The equivalent magnetic current distributions on the two slots are obtained with a MoM procedure assuming that they are radiating in a semi-infinite medium. The geometry of the dielectric lens is then introduced and the magnetic field on the slots due to a double scattering in the internal region of the lens is calculated. The reaction integral between the magnetic currents in the presence of a semi-infinite medium and the magnetic field in the presence of the lens modifies the amplitude of the equivalent magnetic currents on the slots and, therefore, the pertinent input impedance seen by the rest of the circuit. The effect of the lens on the amplitude of the power coupling efficiency is small, but appears to be the source of ripples often visible in the measurements. Moreover, if the antenna is not located within a few micrometers of the geometrical focus of the lens, the ripples disappear from the measurements, and this effect is also confirmed by the calculations obtained with the model. When the antenna is located slightly off the focus, the “focusing” effect of the lens on the phase of the impinging rays is not coherent any more, and all the rays do not recombine in phase. The result on the shape of the efficiency curve is like an “averaging” effect and the ripples disappear.

The next feature that has been introduced into the model is the limited field of view of the antenna due to the dimensions of the antenna chip itself. With reference again to Fig. 4, starting from the center of the antenna chip, the chip itself extends for 1.2 mm

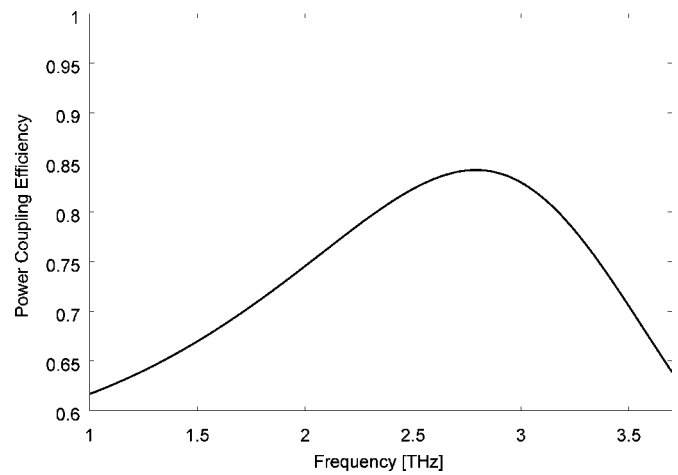


Fig. 8. Power coupling efficiency between a 2.5-THz twin-slot antenna and the silicon lens versus frequency.

on the E -plane and 0.6 mm on the H -plane. According to this geometry and to its thickness, and considering the first-order approximation in terms of geometrical optics, all the power radiated by the antenna at angles smaller than α on the E -plane and β on the H -plane does not directly reach the lens because of the proximity of the edges of the antenna chip. Conversely, any power coupled to the lens within these angles does not reach the antenna. Therefore, there is no optical coupling between antenna and silicon lens in these two regions. In our setup, $\alpha = 17.6^\circ$ and $\beta = 32.4^\circ$. In Fig. 4, the gray areas highlights these regions. Only the 600-GHz detectors have chips that extend for 1.2 mm on both planes, therefore, in this case, the smaller angle applies on both principal planes. Obviously, this limit on the field of view of the antenna has repercussions on the power coupling efficiency between antenna and lens. A calculation of the power coupling efficiency due to this effect for a 2.5-THz design is shown in Fig. 8. The graph represents the amount of power that is collected by the antenna versus frequency. This contribution has been calculated by integrating the antenna pattern on a limited field of view, imposed by the geometry of the antenna chip, rather than on a 180° span. Between 2.5–3 THz, roughly 85% of the power is collected by the antenna, but this figure goes down to almost 60% at 1 THz. The radiation pattern of the twin-slot antenna into the silicon lens is shown in Fig. 9 where the gray zones indicate the blind spots of the antenna on the two principal planes.

Next, the complex characteristic impedance and propagation constant of the CPW lines are calculated taking into account both radiation and conduction losses. The parameters of the transmission lines are first obtained using the formalism presented in [8] assuming infinitely thin metal and no ohmic losses. The unknown magnetic currents are obtained from the direct solution of the pertinent continuity of magnetic field integral equation (CMFIE) assuming, as in [13], the separability between transverse and longitudinal space functional dependence. In particular, the transverse electric field is assumed to be well represented by a unique edge singular function defined on each of the two slots composing the CPW. The procedure for finding the space domain magnetic current consists of: 1) expanding via a Fourier transform the transverse impressed magnetic field in

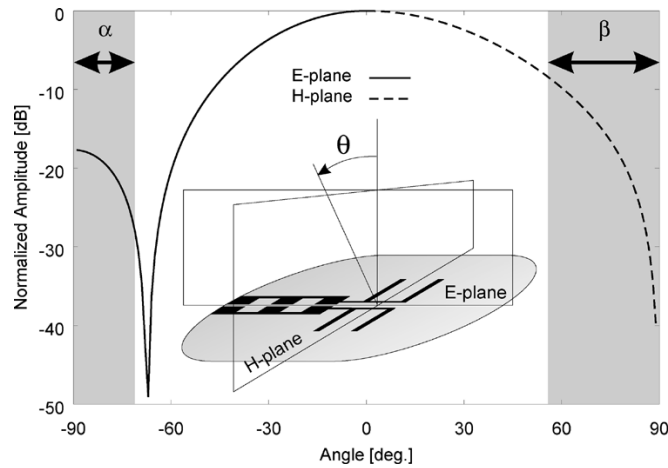


Fig. 9. Calculated twin-slot antenna radiation pattern in the silicon lens at 2.5 THz with the indication of the blind spots on both principal planes.

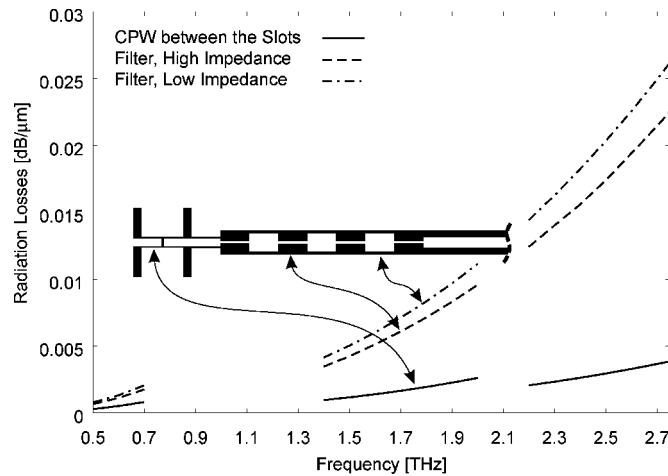


Fig. 10. Summary of radiation losses along the CPW lines versus frequency. In this figure, the level of losses is reported for each of the three different CPW lines in each of the four designed bands.

spectral superposition of electric currents progressively phased by k_x ; 2) finding in analytical form, for each k_x , the two-dimensional (2-D) Green's function (GF) by imposing the continuity of the magnetic field at the slot axis; and 3) integrating in k_x all the 2-D GF. Equating to zero the denominator of the spectral expression for the magnetic currents, a dispersion equation is obtained that, solved numerically, defines the propagation constant of the leaky mode supported by the structure. We then introduce the conduction losses resorting to the formulation presented in [14] and considering a measured gold film resistivity of $0.55 \mu\Omega \cdot \text{cm}$ and a metal thickness of $0.3 \mu\text{m}$. The parameters of the CPW allow us to transform the input impedance of the slots to the bolometer section and to calculate the equivalent input impedance seen by the bolometer. Fig. 10 shows a summary of the different radiation losses that occur in the three CPW lines involved in each circuit. In this figure, starting from the lowest frequency, we have the level of radiation losses produced by the three CPW lines in the 600-GHz design, we then have the case of the 1.6- and 1.8-THz design and, finally, the 2.5-THz design, which, of course, has a higher level of losses.

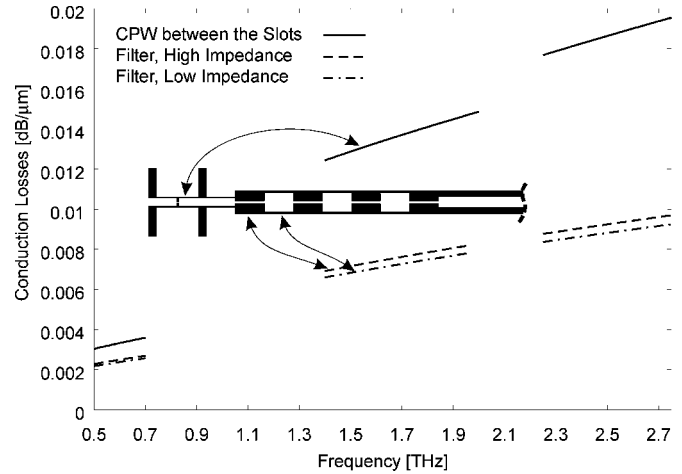


Fig. 11. Summary of conduction losses along the CPW lines versus frequency. In this figure, the level of losses is reported for each of the three different CPW lines in each of the four designed bands.

In each case, the losses are expressed in decibels/micrometer. From this figure, it is apparent that the CPW line between the slots gives the smallest contribution to the radiation losses, while the RF filter contributes the most. Fig. 11 shows a similar summary for the conduction losses. From this figure, it is apparent that the same CPW line that before was giving the smallest contribution to the radiation losses now contributes the most to conduction losses. Putting together both mechanisms for the losses, on average, each part of the circuit gives more or less the same total contribution.

The effect of the reactances due to the bolometer transition is the next step. Whether the transition is tapered or nontapered, the bolometer width is much narrower than the width of the CPW inner conductor, and a strong inductive load is concentrated at this section of the circuit, especially in the tapered case. This model accounts for the effect of the transition by combining two equivalent lumped reactances related to the length and width of the transition itself. An inductive reactance is derived by investigating the canonical slot problem that best fits the length of the gap. The value of this inductance also depends on the actual shape of the transition. Finally, the expression for the inductance is evaluated analytically. A detailed description of the analytical formulation can be found in [8] and the references therein.

Last but not least, there is the RF choke filter. This consists of seven high- and low-impedance sections and is designed to present a “short circuit” for the RF current at the interface with the radiating slot. Actually, the impedance that is presented to the slot in the equivalent circuit is close to zero for the real part, but not for the imaginary part. Therefore, when the filter impedance is transformed along the Smith chart up to the bolometer section of the circuit, an even bigger impedance is typically found. In particular, even if the real part does not produce a considerable effect at the bolometer section, the imaginary part has a rather big impact on the resonating properties of the circuit and, therefore, on the center frequency of the detector. In this procedure, the filter is modeled in terms of a sequence of CPW line sections, where the characteristic

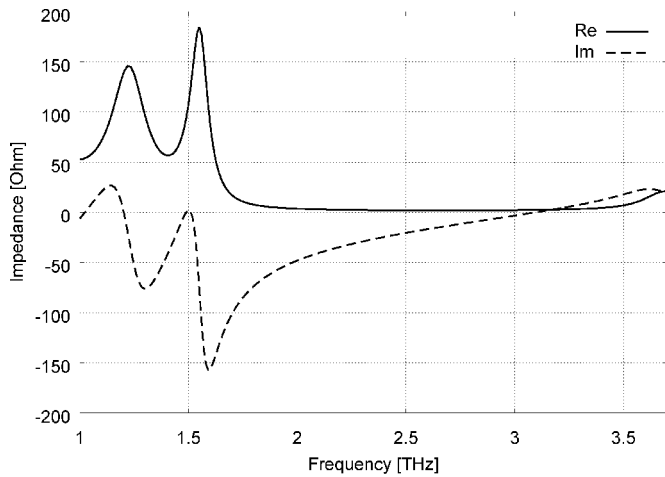


Fig. 12. Calculated real and imaginary part of the input impedance of the RF choke filter at the left-hand-side slot section of Fig. 1(b).

impedance and propagation constant of each section are calculated using the same formalism described earlier.

Once all the different parts of the detector have been accurately modeled, the amount of power dissipated in the bolometer versus the total power provided to the detector can be calculated.

IV. DESIGN IMPROVEMENTS

Starting from an earlier design, based on a previous simplified model [6], several modifications have been made to improve the performance in terms of overall power coupling efficiency and center frequency. First, the slot length has been decreased from one full wavelength to a half-wavelength in order to obtain a better impedance match to the bolometer resistance. A full-wavelength slot typically presents a low input impedance at its center that transforms into a high impedance at the bolometer through the quarter-wavelength section of CPW line. Considering that bolometer resistances of $\sim 20 \Omega$ have been shown to provide the best performance, we chose to use shorter slots. A half-wavelength slot presents a high input impedance (roughly $180\text{--}190 \Omega$ at 2.5 THz) that transforms in a low impedance (around 10Ω) at the bolometer, thus providing a much better impedance matching efficiency. The full-wavelength slots were originally chosen for the symmetry of their radiation patterns. However, simulations performed on the beam pattern of the new designs have shown that, even in this case, the pattern on the two principal planes (E - and H -plane) are close enough to provide a good coupling with the elliptical lens.

The RF choke filter has also been modified. The length of the different sections of the filter has been adjusted to better tune the center frequency. As shown in Fig. 12 for a 2.5-THz detector, the real part of the impedance the filter presents at the edge of the left-hand-side slot section [see Z_f in Fig. 1(b)] is indeed very close to a short circuit, as required to block RF leakage. However, the imaginary part is not necessarily zero in the same bandwidth. Also shown in Fig. 12 is the imaginary part of the filter impedance that, in this case, presents a capacitive load at 2.5 THz. Once transformed at the bolometer section through a quarter-wavelength CPW section, this capacitive load typically turns inductive and is primarily responsible for the down shift

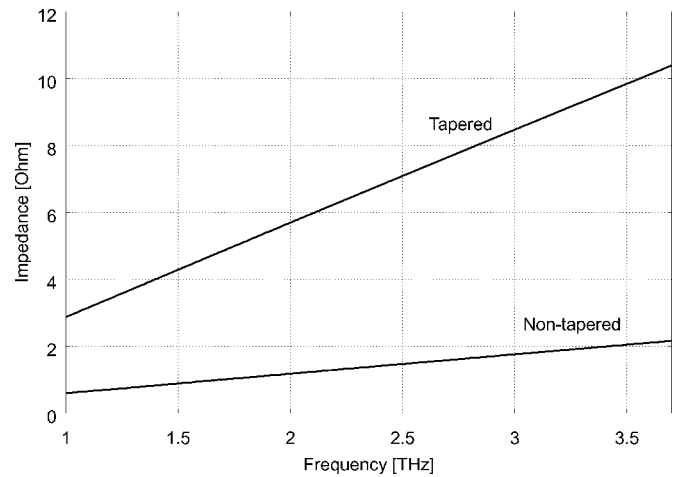


Fig. 13. Calculated input reactances for tapered and nontapered bolometer transitions for a 2.5-THz detector.

in the center frequency observed in earlier designs. Therefore, the effect of the filter must be taken into account to properly determine the center frequency of the detector. In particular, this impedance depends strongly on the length of its first section L_O and, by tuning this length, we adjust the center frequency, also depending on the bolometer transition used (see Fig. 3 for the different lengths used in the designs). In the new model, the number of high- and low-impedance sections has been reduced from 8 to 7 and the transition between antenna and filter has also been changed from tapered to nontapered. Moreover, the choice of using higher impedance slots is also intended to make the embedding circuit less sensitive to unexpected impedance variations like those introduced by the filter. Since these two elements are in series (see Fig. 5), the effect of the filter impedance on the embedding circuit is smaller when it is in series with a high impedance like the one of a half-wavelength slot.

The shape of the bolometer transition has also been modified. Based on the formulation presented in [8], a nontapered transition, as shown in Fig. 2(b), has been adopted. Despite the physical appearance, a nontapered transition has a much lower impact on the embedding impedance. The equivalent impedance of the transition is directly proportional to its length, therefore, the shorter the better. Fig. 2 shows a sample of the two different transitions used in the new designs. The traditional tapered transition has also been included in the new design for comparison with the nontapered results. Fig. 13 shows an example of the calculated input impedance (purely imaginary) of tapered and nontapered transitions for a 2.5-THz detector. The inductive impedance shown by both transitions is in series with the rest of the circuit and tends to lower the center frequency of the detector even further than what the filter already does. It is evident how the nontapered case has a much smaller effect on the overall embedding impedance seen by the bolometer. In particular, the effect of the nontapered transition is approximately 80% lower than the tapered one, thus limiting the down shift in the center frequency.

Fig. 14 finally shows a comparison between the old and new design at 2.5 THz. The effect of the improvements discussed here on the geometry are clearly visible in the two photographs taken with the SEM. Also, improvements in the fabrication

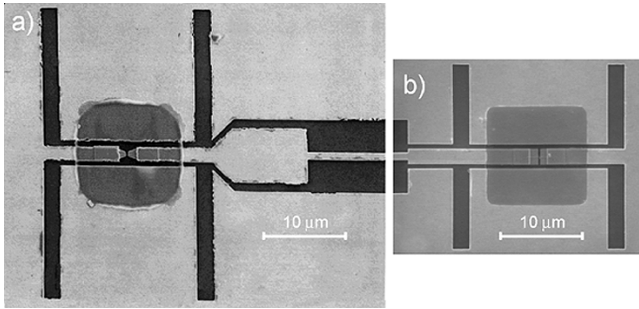


Fig. 14. Comparison between: (a) old and (b) new design for a 2.5-THz detector. The two SEM photographs have the same scale.

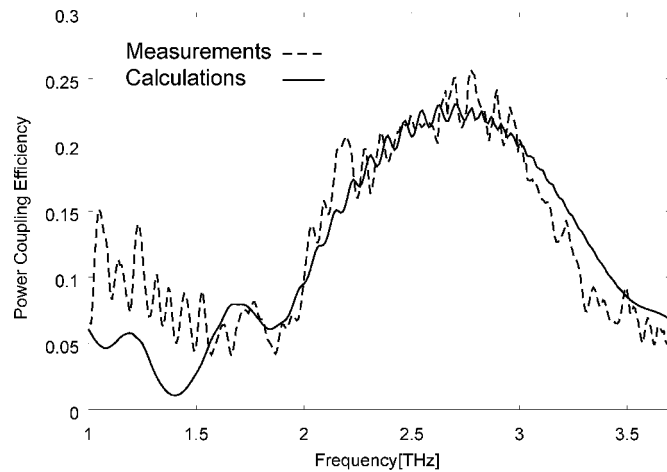


Fig. 15. Calculated and measured power coupling efficiency versus frequency of a 2.5-THz detector with a 0.1- μm bolometer, tapered transition, and measured bolometer dc resistance of 16 Ω .

process have resulted in sharp well-defined circuit edges. The bolometer region, for instance, now features a flawless nontapered transition with a 0.1- μm -wide gap across a 2- μm -wide CPW inner conductor.

V. MEASURED AND CALCULATED DATA

All the measurements have been performed with a high-resolution Bruker HR-120 FTS using a 23- μm -thick Mylar beam splitter for all the frequency bands, except for the lowest one. For the 600-GHz detectors, a 50- μm beam splitter has instead been used, having a better frequency response in that range. Moreover, before comparing measurements with calculations, the measured data have been corrected for the frequency response of the beam splitter itself, for the presence of a 50- μm -thick Mylar window in our Dewar, and for the frequency overmoding of the optical beam impinging on the silicon lens. The physical temperature of the mixer block is 4.2 K. In order to better compare the data, the amplitude of the measured data has also been normalized to the same level of the calculated data since the FTS measures only a relative spectral response.

Fig. 15 shows the overall power coupling efficiency versus frequency of a 2.5-THz detector with a 0.1- μm bolometer, a tapered transition, and a measured bolometer dc resistance of 16 Ω . The prediction obtained with this model agrees very well with the measurements both in terms of center frequency and

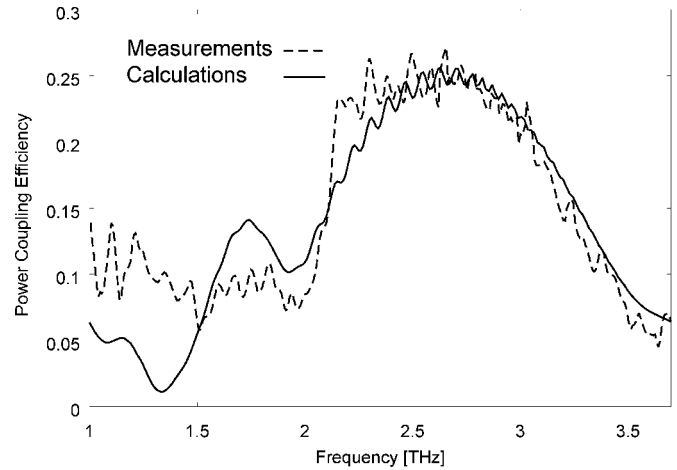


Fig. 16. Calculated and measured power coupling efficiency versus frequency of a 2.5-THz detector with a 0.1- μm bolometer, nontapered transition, and measured bolometer dc resistance of 18 Ω .

f_c Design [THz]	f_c Measured [THz]	f_c Avg. Error [%]	BW Design [THz]	BW Measured [THz]	BW Avg. Error [%]
2.70	2.63 \pm 1.1%	+4.2%	1.36 \pm 5.8%	1.19 \pm 7.5%	+14.2%
1.95	1.87 \pm 1.6%	+4.2%	1.03 \pm 1.9%	0.87 \pm 1.1%	+18.3%
1.72	1.86 \pm 2.1%	-7.5%	0.89 \pm 3.3%	0.77 \pm 6.4%	+15.5%
0.62	0.63 \pm 3.1%	-1.5%	0.33 \pm 0.1%	0.28 \pm 0.7%	+17.8%

Fig. 17. Summary of all measured and calculated data for center frequency and bandwidth along with percentage errors.

bandwidth. The model has also been able to predict with a considerable accuracy the rolloff at higher frequencies, the dip at 1.9 THz, and the secondary peak at 1.7 THz. Moreover, according to our model, less than 25% of the total power provided to the detector is actually dissipated on the bolometer. This result is in very good agreement with earlier measurements done at the Jet Propulsion Laboratory (JPL), Pasadena, CA, where the total power loss in this kind of detector was shown to be around 6 or 7 dB [3].

Fig. 16 shows the result for the case where the bolometer has a nontapered transition and the bolometer resistance has been measured to be 18 Ω . Again, the agreement is very good and the model was able to predict all the features of the frequency response with an excellent accuracy. It is particularly worth noting how changing just the bolometer transition changes the performance of the detector, especially between 1.5–2 THz.

A summary of all measured and calculated data for center frequencies and bandwidths along with the pertinent percentage errors is reported in the table shown as Fig. 17. A total of 21 detectors, evenly distributed among the four different frequency bands, have been measured in producing the results shown in this figure. For instance, if we consider the first row of this figure, for a calculated center frequency of 2.7 THz, we measured 2.63 \pm 1.1%, giving an average error of 4.2%. Continuing for the bandwidth: for a calculated value of 1.36 THz \pm 5.8%, depending on tapered or nontapered transition and 0.1- or 0.2- μm -long bolometers, we measured 1.19 \pm 7.5% for an average error of less than 15%. Considering that we are describing the performance of a planar circuit at 2.7 THz, with a bandwidth larger than 1 THz, we believe it is a reasonably good result. In average, we were always able to

predict the center frequency with an error smaller than 5% and the bandwidth with an error around 15%. These results would already be good at 100 GHz, but at 2.5 THz, they represent a significant improvement in circuit design capability.

VI. CONCLUSIONS

In this paper, we presented an accurate electromagnetic model to predict the performance of terahertz mixers and detectors. Starting from a simplified model, a computer code able to simulate the effect of all the parts of the circuit has been developed. The adopted formulation is based on a spectral-domain analysis of the electromagnetic problem resulting, in many cases, in numerically efficient closed-form expressions. The code exploits the MoM to calculate the input impedance of the twin slots in a simplified configuration (i.e., with a semi-infinite medium rather than a silicon lens in front of the antenna), and then the contributions of all the other parts of the detector and circuit are introduced: the Gaussian beam coupling, reflection at the lens interface, double scattering inside the lens, limited field of view of the antenna, radiation and conduction losses in the CPW lines, bolometer transition, and RF choke filter. Finally, the power dissipated in the bolometer is calculated, allowing a direct comparison with measured data.

The reliability of this model has been demonstrated by the extensive set of measurements performed in our laboratories. The measurements have also proven that the model is not only accurate and reliable for the analysis of such detectors, but also for the synthesis and design, as shown by the excellent agreement between measurements and calculations. Moreover, this same model can be easily applied to detectors based on stratified media and is accurate and reliable both at low (600 GHz) and high (2.5 THz) frequencies.

It is also important to note that the model described in this paper can also be used to design embedding circuits for detectors based on different devices such as SIS mixers and Schottky mixers as long as the required impedance is between a few ohms and a few hundred ohms.

Even though the model is already quite accurate, we are working on further improvements. In particular, we want to substitute the approximated Gaussian beam pattern of the silicon lens with its actual radiation pattern. The procedure to do that [15] is not straightforward and requires some additional work. Nonetheless, the model gave us very good results even in this version.

To conclude, we believe that this model is very useful in the analysis and design of terahertz mixers and detectors. It has been demonstrated by the measurements shown in this paper, especially considering the unprecedented accuracy this model reached in predicting the performance of HEB mixers both in terms of center frequency and bandwidth from 600 GHz to 2.5 THz.

ACKNOWLEDGMENT

The authors wish to thank B. Bumble and R. LeDuc, both of the Jet Propulsion Laboratory (JPL), California Institute of Technology, Pasadena, for fabricating the new detectors.

This research was carried out at the JPL, California Institute of Technology.

REFERENCES

- [1] D. B. Rutledge, D. P. Neikirk, and D. P. Kasiligan, "Integrated circuit antennas," in *Infrared and Millimeter-Waves*, K. J. Button, Ed. New York: Academic, 1983, vol. 10, pp. 1–90.
- [2] D. F. Filipovic, S. S. Gearhart, and G. M. Rebeiz, "Double slot antennas on extended hemispherical and elliptical silicon dielectric lenses," *IEEE Trans. Microw. Theory Tech.*, vol. 41, no. 10, pp. 1738–1749, Oct. 1993.
- [3] B. S. Karasik, M. C. Gaidis, W. R. McGrath, B. Bumble, and H. G. LeDuc, "Low noise in a diffusion-cooled hot-electron mixer at 2.5 THz," *Appl. Phys. Lett.*, vol. 71, p. 1567, 1997.
- [4] W. F. M. Ganzevles, L. R. Swart, J. R. Gao, P. A. J. de Korte, and T. M. Klapwijk, "Direct response of twin-slot antenna-coupled hot-electron bolometer mixers designed for 2.5 THz radiation detection," *Appl. Phys. Lett.*, vol. 76, no. 22, pp. 3304–3306, May 2000.
- [5] J. Kawamura, T. R. Hunter, C.-Y. E. Tong, R. Blundell, D. C. Papa, F. Patt, W. Peters, T. L. Wilson, C. Henkel, G. Gol'tsman, and E. Gershenson, "Ground-based terahertz CO spectroscopy toward Orion," *Astron. Astrophys.*, vol. 394, pp. 271–274, 2002.
- [6] R. A. Wyss, A. Neto, W. R. McGrath, B. Bumble, and H. LeDuc, "Submillimeter-wave spectral response of twin-slot antennas coupled to hot electron bolometers," in *Proc. 11th Int. Space Terahertz Technology Symp.*, Ann Arbor, MI, May 1–3, 2000, pp. 379–388.
- [7] K. C. Gupta, *Microstrip Lines and Slotlines*, R. Garg and I. J. Bahl, Eds. Norwood, MA: Artech House, 1979.
- [8] P. Focardi, A. Neto, and W. R. McGrath, "Coplanar-waveguide-based terahertz hot-electron-bolometer mixers—Improved embedding circuit description," *IEEE Trans. Microw. Theory Tech.*, vol. 50, no. 10, pp. 2374–2383, Oct. 2002.
- [9] A. Neto, P. J. I. De Maagt, and S. Maci, "Optimized basis functions for slot antennas excited by coplanar waveguides," *IEEE Trans. Antennas Propag.*, vol. 51, no. 7, pp. 1638–1646, Jul. 2003.
- [10] P. F. Goldsmith, *Quasioptical Systems*. Piscataway, NJ: IEEE Press, 1998.
- [11] M. Van der Vorst, P. J. I. De Maagt, A. Neto, A. Reynolds, W. Luinge, R. Heres, and M. Herben, "Effect of the internal reflection on the radiation properties and input impedance of integrated lens antennas: Comparisons between theory and measurements," *IEEE Trans. Microw. Theory Tech.*, vol. 49, no. 6, pp. 1118–1125, Jun. 2001.
- [12] A. Neto, D. Pasqualini, A. Toccafondi, and S. Maci, "Mutual coupling between slots printed at the back of elliptical dielectric lenses," *IEEE Trans. Antennas Propag.*, vol. 47, no. 10, pp. 1504–1507, Oct. 1999.
- [13] D. R. Jackson, F. Mesa, M. J. Freire, D. P. Nyquist, and C. Di Nallo, "An excitation theory for bound modes and residual-wave currents on stripline structures," *Radio Sci.*, vol. 35, no. 2, pp. 495–510, Mar.–Apr. 2000.
- [14] G. Ghione, "A CAD-oriented analytical model for the losses of general asymmetric coplanar lines in hybrid and monolithic MICs," *IEEE Trans. Microw. Theory Tech.*, vol. 41, no. 9, pp. 1499–1510, Sep. 1993.
- [15] D. Pasqualini and S. Maci, "High-frequency analysis of integrated dielectric lens antennas," *IEEE Trans. Antennas Propag.*, vol. 52, no. 3, pp. 840–847, Mar. 2004.



Paolo Focardi received the Doctor degree in electronic engineering and Ph.D. degree in computer science and telecommunication engineering from the University of Florence, Florence, Italy, in 1998 and 2002 respectively.

From 1999 to 2000, he was involved with the final operative phases of the Shuttle Radar Topography Mission (SRTM). In 2001, he spent seven months with the Jet Propulsion Laboratory, California Institute of Technology, Pasadena, where he was involved with the development of HEB mixers for astronomical observations at terahertz frequencies. In 2002, he joined again the staff of the Jet Propulsion Laboratory, as a Post-Doc. He is currently at Jet Propulsion Laboratory where he has a Staff position since 2004. His research is focused on analytical and numerical methods in electromagnetics.

Dr. Focardi was the recipient of the 2002 Microwave Engineering Center for Space Applications (MECSA) Award for the best paper presented at the National Conference on Electromagnetics (RiNem) Conference.



William R. McGrath (M'88) received the B.S. degree in physics from the Massachusetts Institute of Technology (MIT), Cambridge, in 1978, and the M.A. and Ph.D. degrees in physics from the University of California at Berkeley, in 1981 and 1985, respectively.

He is currently a Senior Research Scientist and Group Supervisor with the Jet Propulsion Laboratory, California Institute of Technology, Pasadena. He heads a research group that develops superconductive HEB mixers and direct detectors for terahertz remote-sensing applications. He has authored or coauthored over 170 publications in this field. His research over the last 20 years has focused primarily on superconductive detectors and circuits. This research has involved the development of ultra-low noise SIS and HEB mixers at frequencies up to 2.5 THz.



Andrea Neto received the Doctor degree (*cum laude*) from the University of Florence, Florence, Italy, in 1994, and the Ph.D. degree from the University of Siena, Siena, Italy, in 2000, both in electronic engineering.

He spent almost three years with the Antenna Section of the European Space Agency (ESA) Research and Technology Center (ESTEC). In 2000 and 2001, he was with the Sub-Millimeter Wave Advanced Technology Group, Jet Propulsion Laboratory, California Institute of Technology, Pasadena. Since 2002, he has been with the Center for Applied Scientific Research (TNO), TNO Defence and Security, Den Haag, The Netherlands. His research is focused on analytical and numerical methods in electromagnetism with emphasis on the analysis of large arrays and integrated-circuit and antennas.